GRAPHENE

Emergent ferromagnetism near three-quarters filling in twisted bilayer graphene

Aaron L. Sharpe[1,2]*, Eli J. Fox[2,3]*, Arthur W. Barnard[3], Joe Finney[3], Kenji Watanabe[4], Takashi Taniguchi[4], M. A. Kastner[2,3,5,6], David Goldhaber-Gordon[2,3]†

When two sheets of graphene are stacked at a small twist angle, the resulting flat superlattice minibands are expected to strongly enhance electron-electron interactions. Here, we present evidence that near three-quarters ($^3/_4$) filling of the conduction miniband, these enhanced interactions drive the twisted bilayer graphene into a ferromagnetic state. In a narrow density range around an apparent insulating state at $^3/_4$, we observe emergent ferromagnetic hysteresis, with a giant anomalous Hall (AH) effect as large as 10.4 kilohms and indications of chiral edge states. Notably, the magnetization of the sample can be reversed by applying a small direct current. Although the AH resistance is not quantized, and dissipation is present, our measurements suggest that the system may be an incipient Chern insulator.

In weakly dispersing bands, electron-electron interactions dominate over kinetic energy, often leading to interesting correlated phases. Graphene has emerged as a preeminent platform for investigating such flat bands because of the control of the band structure enabled by stacking multiple layers and the tunability of the band filling via electrostatic gating. In particular, the moiré superlattice of so-called "magic-angle" twisted bilayer graphene (TBG), in which one monolayer graphene sheet is stacked on top of another with a relative angle of rotation between the two crystal lattices of near 1°, is predicted to host nearly flat bands of ~10-meV width (*1*–*3*).

In the single-particle picture, the flat bands are fourfold degenerate because of spin and valley symmetries (*4*). However, magic-angle TBG has recently been shown to exhibit high-resistance states at half ($^1/_2$) and three-quarters ($^3/_4$) filling of the conduction and valence bands (*5*, *6*) and at one-quarter ($^1/_4$) filling of the conduction band (*6*), all cases where metallic behavior would be expected in the absence of interactions. It is notable that magic-angle TBG can become superconducting when doped slightly away from $^1/_2$ filling of either the conduction or valence band (*6*, *7*).

Theoretical calculations have raised the possibility of magnetic order as a result of interactions lifting spin and valley degeneracies (*8*–*15*). Here, we present unambiguous experimental evidence of emergent ferromagnetism at $^3/_4$ filling of the conduction band in TBG: a giant anomalous Hall (AH) effect that displays hysteresis in magnetic field. We also find evidence of chiral edge conduction. Our results suggest that the $^3/_4$-filling state is a correlated Chern insulator.

We used a "tear-and-stack" dry-transfer method (*4*, *16*) and standard lithographic techniques to fabricate a TBG Hall bar device (Fig. 1A, inset) with a target twist angle $\theta = 1.17°$. The graphene is encapsulated in two hexagonal boron nitride (hBN) cladding layers to protect the channel from disorder and to act as dielectrics for electrostatic gating. With both a silicon back gate and Ti/Au top gate, we can independently tune the charge density n in the TBG and the perpendicular displacement field D (*17*, *18*).

We measured the longitudinal and Hall resistances using standard lock-in techniques with a 5-nA root mean square (RMS) ac bias current. A complicated electronic structure is revealed by the behavior of the longitudinal resistance as a function of n and D (Fig. 1A). We observe strong resistance peaks at the charge neutrality point (CNP) [identified from Landau fan diagrams (*17*)] and at densities $\pm n_s = 3.37 \times 10^{12}$ cm^{-2} corresponding to full filling of the mini-Brillouin zone (mBZ) of the TBG superlattice, with four electrons (or holes) per superlattice unit cell. This value of n_s is consistent with a twist angle $\theta = 1.20° \pm 0.01°$ in the TBG heterostructure (*19*), very near our target angle of 1.17°. A slight kink in the positions of the CNP and other features as a function of displacement field is noticeable but not repeatable between cooldowns (*17*).

Beyond the peaks expected from a single-particle picture of the TBG band structure, we observe additional high resistance states at $^1/_4$, $^1/_2$, and $^3/_4$ fillings of the mBZ. These fillings, corresponding to one, two, and three electrons per superlattice unit cell, respectively, have previously been attributed to correlated insulating states (*6*, *7*). Another unexpected peak at $n/n_s = -1.15$ and a corresponding shoulder on the full filling peak of the electron side (Fig. 1B) do not correspond to expectations for TBG alone. They likely result from the lattice alignment of the top graphene sheet with the top hBN layer, with the density $1.15n_s$ corresponding to an angle $\theta = 0.81° \pm 0.02°$ (*19*). Such near-alignment with the top hBN layer is confirmed in an optical image of the heterostructure (fig. S1) by the rotational alignment of straight edges of the hBN and graphene flakes; the bottom hBN is far from aligned with the bottom graphene sheet. This vertical asymmetry in the heterostructure may play a role in the strong dependence of the peak structure on the sign and magnitude of the displacement field (*17*).

Magnetotransport in graphene-based heterostructures typically does not depend on the history of the applied field. However, we find that in a narrow range of n near $n/n_s = {}^3/_4$, transport is hysteretic with respect to an applied out-of-plane magnetic field B (Fig. 2A). When the applied field is swept to zero from a large negative value, a large AH resistance $R_{yx} \approx \pm 6$ kilohms remains, with the sign depending on the direction of the field sweep, indicating that the sample has a remanent magnetization. This large AH signal is notable given the absence of both transition metals (typically associated with magnetism) and heavy elements (to give spin-orbit coupling) in TBG. If the field is left at zero, the magnetization is very stable, with no substantial change in the Hall resistance observed over the course of 6 hours (*17*). As the field is increased beyond a coercive field on the order of 100 mT opposite to the direction of the training field, the Hall signal changes sign, pointing to a reversal of the magnetization.

Multiple intermediate jumps appear near the coercive field; these are very repeatable over successive hysteresis loops (*17*) and likely correspond to either a mixed domain structure with varying coercivities or a repeatable pattern of domain wall motion and pinning. This behavior may result from inhomogeneity caused by local variations in the twist angle between the graphene sheets, which has recently been directly imaged using transmission electron microscopy (*20*), or by local variations in electrostatic potential (*21*).

Hysteresis loops of R_{yx} and R_{xx} would ideally be antisymmetric and symmetric, respectively [in the sense that $R_{ij}(B) = \pm\tilde{R}_{ij}(-B)$, where R_{ij} and $\tilde{R}_{ij}$ are measured with the field sweeping in opposite directions]. We find that R_{yx} hysteresis loops are roughly antisymmetric but offset vertically by −1 kilohms. R_{xx} is nearly flat with field but has an antisymmetric component, presumably because of mixing-in of the large changes in R_{yx}.

We define the coercive field as half the difference between the fields where the largest jumps in R_{yx} occur on the upward and downward sweeps. With increasing temperature T, the coercive field steadily decreases before vanishing at 3.9 K (Fig. 2, C and D). This monotonic dependence is

[1]Department of Applied Physics, Stanford University, 348 Via Pueblo Mall, Stanford, CA 94305, USA. [2]Stanford Institute for Materials and Energy Sciences, SLAC National Accelerator Laboratory, 2575 Sand Hill Road, Menlo Park, CA 94025, USA. [3]Department of Physics, Stanford University, 382 Via Pueblo Mall, Stanford, CA 94305, USA. [4]National Institute for Materials Science, Namiki 1-1, Tsukuba, Ibaraki 305-0044, Japan. [5]Science Philanthropy Alliance, 480 California Avenue #304, Palo Alto, CA 94306, USA. [6]Department of Physics, Massachusetts Institute of Technology, 77 Massachusetts Avenue, Cambridge, MA 02139, USA.
*These authors contributed equally to this work.
†Corresponding author. Email: goldhaber-gordon@stanford.edu

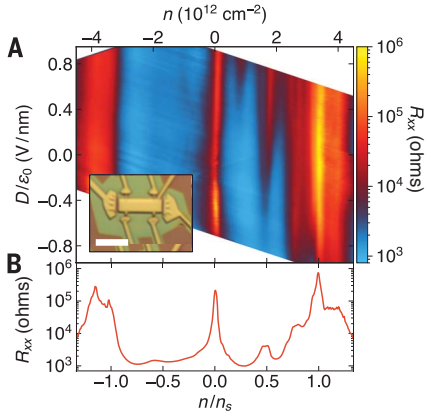

Fig. 1. Correlated states in near-magic-angle TBG. (**A**) Longitudinal resistance R_{xx} of the TBG device (measured between contacts separated by 2.15 squares) as a function of carrier density n (shown on the top axis) and perpendicular displacement field D (left axis), which are tuned by the top- and back-gate voltages, at 2.1 K. n is mapped to a filling factor relative to the superlattice density n_s, corresponding to four electrons per moiré unit cell, shown on the bottom axis. (Inset) Optical micrograph of the completed device showing the top-gated Hall bar region (gold), electrical contacts (gold), regions of the heterostructure that have been etched to remove the TBG (green), and regions of the heterostructure that have not been etched (brown). Scale bar, 5 μm. (**B**) Line cut of R_{xx} with respect to n taken at $D/\epsilon_0 = -0.22$ V/nm showing the resistance peaks at full filling of the superlattice and additional peaks likely corresponding to correlated states emerging at intermediate fillings.

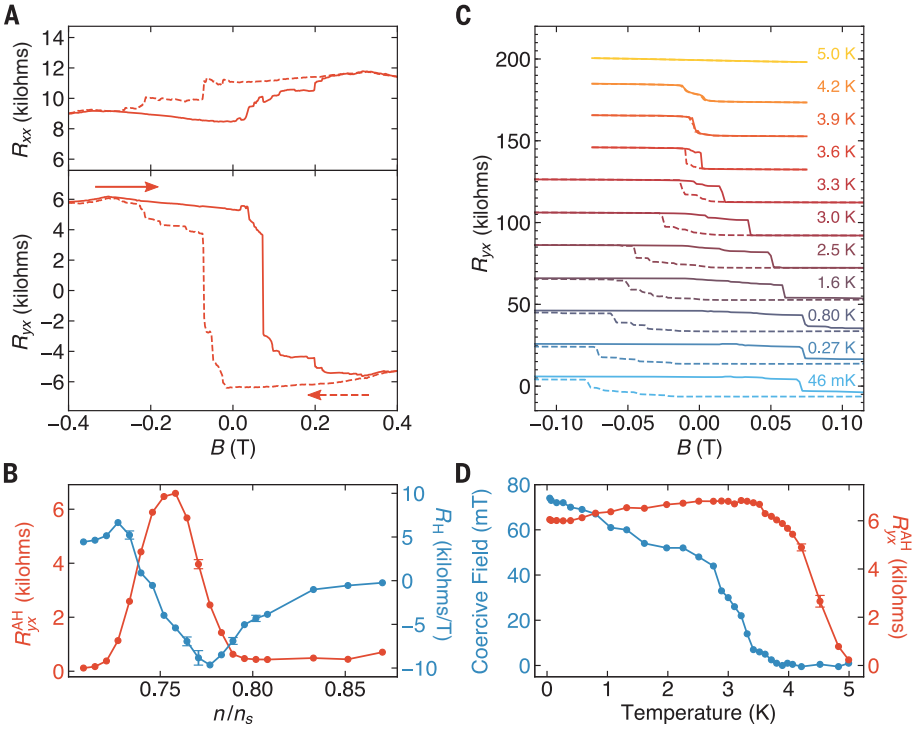

Fig. 2. Emergent ferromagnetism near three-quarters filling. (**A**) Magnetic field dependence of the longitudinal resistance R_{xx} (upper panel) and Hall resistance R_{yx} (lower panel) with $n/n_s = 0.746$ and $D/\epsilon_0 = -0.62$ V/nm at 30 mK, demonstrating a hysteretic AH effect resulting from emergent magnetic order. The solid and dashed lines correspond to measurements taken while sweeping the magnetic field B up and down, respectively. (**B**) Zero-field AH resistance R_{yx}^{AH} (red) and ordinary Hall slope R_H (blue) as a function of n/n_s for $D/\epsilon_0 \approx -0.6$ V/nm. R_{yx}^{AH} is peaked sharply with a maximum around $n/n_s = 0.758$, coincident with R_H changing sign. These parameters are extracted from line fits of R_{yx} versus B on the upward and downward sweeping traces in a region where the B-dependence appears dominated by the ordinary Hall effect (*17*). The error bars reflect fitting parameter uncertainty along with the effect of varying the fitting window and are omitted when smaller than the marker. (**C**) Temperature dependence of R_{yx} versus B at $D/\epsilon_0 = -0.62$ V/nm and $n/n_s = 0.746$ between 46 mK and 5.0 K, showing the hysteresis loop closing with increasing temperature. Successive curves are offset vertically by 20 kilohms for clarity. (**D**) Coercive field and AH resistance (extracted using the same fitting procedure as above) plotted as a function of temperature from the same data partially shown in (C). Data in Fig. 2 were taken during a separate cooldown from that of the data in the rest of the figures but show representative behavior (*17*).

expected because flipping individual domains or moving domain walls in a magnet is usually thermally activated (*22*).

The Hall signal appears to be the sum of two parts: an anomalous component that reflects the sample magnetization (*23*), and a conventional component linear in field with a Hall slope R_H (Fig. 2B) [see (*17*) for how we separate these two components]. Unlike the coercive field, the magnitude of the residual AH resistance at zero field, which we denote by R_{yx}^{AH}, does not vary monotonically with temperature: R_{yx}^{AH} rises slightly with increasing T up to 2.8 K before rapidly falling to zero by 5 K (Fig. 2, C and D).

Although the hysteresis is observable over a wide range of displacement fields (*17*), it only emerges in a narrow range of densities near $^3/_4$ filling of the mBZ. R_{yx}^{AH} displays a sharp peak as a function of n/n_s, reaching 6.6 kilohms for $n/n_s = 0.758$ with a full width at half maximum of $0.04n_s$ (Fig. 2B). These measurements were made along a trajectory for which D changes by ~10% coincident with the primary intended change in n (*17*). In a separate measurement, we observed hysteresis loops with R_{yx}^{AH} up to 10.4 kilohms (fig. S7B).

The gate-voltage dependence of the conventional linear Hall slope R_H (*17*) appears typical for a transition from p-type– to n-type–dominated conduction in a semimetal or small-gap semiconductor, with $|R_H|$ rising when approaching the transition from either side, then turning over and crossing through zero (Fig. 2B). Recent studies of near-magic-angle TBG have reported high resistance at $^3/_4$ filling (*6*, *7*) (compare with Fig. 1), suggesting that spin and valley symmetries are spontaneously broken, resulting in a low density of states (or a gap) at this filling. Our results similarly indicate a possible correlated insulating state, here with an AH effect in a narrow range of densities around this same filling.

The presence of a giant AH effect in an apparent insulator is reminiscent of a ferromagnetic topological insulator approaching a Chern insulator state (*24*–*26*), where it would exhibit a quantum AH (QAH) effect: longitudinal resistivity ρ_{xx} approaches zero and Hall resistivity ρ_{yx} is quantized to h/Ce^2 (*27*, *28*), where h is Planck's constant, e is the electron charge, and C is the Chern number arising from the Berry curvature of the filled bands ($C = \pm 1$ in presently available QAH materials). Chiral edge modes associated with a quantized Hall system manifest in nonlocal transport measurements (*29*, *30*). In an ideal QAH system described by the Büttiker edge state model (*31*), floating metallic contacts equilibrate with the chiral edge states that propagate into them. Clearly, our results are not those of an ideal QAH system. Dissipation can cause deviations from the ideal behavior, while still giving results differing from classical diffusive transport. Below, we present and analyze our experimental evidence for nonlocal transport in the magnetic state.

The three-terminal resistance $R_{54,14}$, where $R_{ij,k\ell} = V_{k\ell}/I_{ij}$ and $V_{k\ell}$ is the voltage between

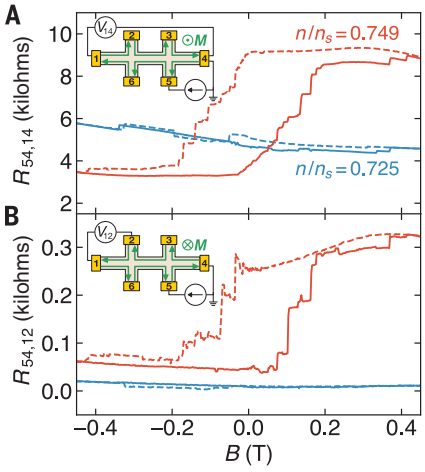

Fig. 3. Nonlocal resistances providing evidence of chiral edge states. (**A** and **B**) Three- and four-terminal nonlocal resistances $R_{54,14}$ (A) and $R_{54,12}$ (B), measured at 2.1 K with $D/\epsilon_0 = -0.22$ V/nm on upward and downward sweeps of the magnetic field (solid and dashed traces, respectively). For $n/n_s = 0.725$ (blue) away from the peak in AH resistance R_{yx}^{AH}, the nonlocal resistances are consistent with diffusive bulk transport. However, with $n/n_s = 0.749$ (red) in the magnetic regime where R_{yx}^{AH} is maximal, large, hysteretic nonlocal resistances suggest chiral edge states are present. (Insets) Schematics of the respective measurement configurations. Green arrows in the upper inset represent the apparent edge state chirality for positive magnetization, whereas in the lower inset they reflect negative magnetization.

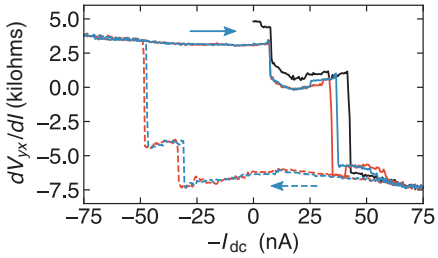

Fig. 4. Current-driven switching of the magnetization. Differential Hall resistance dV_{yx}/dI measured with a 5 nA ac bias as a function of an applied dc bias I_{dc} at 2.1 K with $D/\epsilon_0 = -0.22$ V/nm and $n/n_s = 0.749$. After magnetizing the sample in a −500 mT field and returning to $B = 0$, I_{dc} was swept from 0 to −75 nA (black trace), resulting in dV_{yx}/dI changing sign. Two successive loops in I_{dc} between ±75 nA demonstrate reversible and repeatable switching of the differential Hall resistance (red and blue, with solid and dashed traces corresponding to opposite sweep directions). Note that dV_{yx}/dI is plotted against $-I_{dc}$ for better comparison with magnetic field hysteresis loops.

terminals k and ℓ when a current I_{ij} flows from terminal i to j, is shown in Fig. 3A for two values of n/n_s. When the density is tuned away from the center of the magnetic regime, $R_{54,14}$ is ~5 kilohms and nearly independent of the applied field. We ascribe this behavior to diffusive bulk transport and a finite contact resistance to ground. By contrast, at the center of the magnetic regime, we observe a hysteresis loop with $R_{54,14}^{\downarrow} = 3.3$ kilohms and $R_{54,14}^{\uparrow} = 9.1$ kilohms, where $R_{ij,k\ell}^{\uparrow(\downarrow)}$ are the remanent resistances at zero field after the sample has been magnetized by an upward (downward) applied field [more precisely defined in (*17*) in the discussion of calculating R_{yx}^{AH}]. The difference $|R_{54,14}^{\uparrow} - R_{54,14}^{\downarrow}|$ is largest near the peak in R_{yx}^{AH} shown in Fig. 2B. For a QAH effect, we would expect $R_{54,14}$ to be either 0 or h/Ce^2 (25,813 ohms for $C = 1$). Although the difference $|R_{54,14}^{\uparrow} - R_{54,14}^{\downarrow}| = 5.8$ kilohms is smaller than the ideal $C = 1$ QAH case by a factor of 4, it could be consistent with a QAH state in combination with other dissipative transport mechanisms or a complex network of domain walls (in addition to contact resistance). These three-terminal measurements alone cannot rule out diffusive bulk transport with a very large (anomalous) Hall coefficient, but four-terminal measurements suggest this is unlikely.

In contrast to the three-terminal case, four-terminal nonlocal resistances where the voltage is measured far from the current path are exponentially small in the case of homogeneous diffusive conduction (*32*). For $n/n_s = 0.725$, away from the peak in R_{yx}^{AH}, the measured $R_{54,12} = 10$ ohms (Fig. 3B) is indeed small. In the magnetic regime at $n/n_s = 0.749$, however, the four-terminal resistance is two orders of magnitude larger than the 3 ohms expected from homogeneous bulk conduction, with a hysteresis loop yielding $R_{54,12}^{\downarrow} = 42$ ohms and $R_{54,12}^{\uparrow} = 240$ ohms. Although this four-terminal resistance would be zero in an ideal QAH state with pure chiral edge conduction, the presence of additional conduction paths, such as extra nonchiral edge states (*33*), parallel bulk conduction, or transport along magnetic domain walls (*34*, *35*), can result in large, hysteretic nonlocal resistances [we elaborate on this discussion in (*17*)].

We find that the $n/n_s = {}^3/_4$ state is extremely sensitive to the direction of an applied current. All of the measurements described above were performed with a 5 nA RMS ac bias current, but we observed curious behavior when we added a dc bias I_{dc} to this small ac signal. Sweeping I_{dc} between ±75 nA with $B = 0$ (Fig. 4), we found that the differential Hall resistance dV_{yx}/dI follows a hysteresis loop reminiscent of its magnetic field dependence. This loop was very repeatable after a slight deviation from the first trace (black trace, Fig. 4), for which I_{dc} was ramped from 0 to −75 nA after first magnetizing the sample in a −500 mT field. Additional details about the nature of the jumps in differential resistance and the effect of external magnetic field on the hysteresis loops are presented in (*17*).

The switching of dV_{yx}/dI clearly demonstrates that, like the external magnetic field, the applied dc bias modifies the magnetization. This phenomenon might be similar to switching in other ferromagnetic materials, in which spin-transfer or spin-orbit torques can influence the magnetization. However, the current necessary to flip the moment appears to be very small (*36*). It has also been proposed that a current could efficiently drive domain wall motion in a QAH system owing to quantum interference effects from the edge states (*37*).

Our observation of a large hysteretic AH effect establishes a ferromagnetic moment associated with the apparent ${}^3/_4$ correlated insulating state. Specifically, we suggest that this state is a Chern insulator, with the AH effect arising intrinsically from Berry curvature in the band structure. Extrinsic mechanisms for AH, based on scattering rather than band topology, cannot contribute to the Hall resistance of an insulator (*23*), yet the measured R_{yx}^{AH} is largest at an apparent insulating state. Furthermore, our measurements yield a Hall angle ρ_{yx}/ρ_{xx} up to 1.4, almost an order of magnitude larger than any other reported AH (*38*), apart from magnetic topological insulators exhibiting a QAH effect (here, we convert our measured resistances to resistivities, which we approximate as spatially homogeneous). With $\rho_{yx} \lesssim 0.4h/e^2$ and $\rho_{xx} \approx 0.3h/e^2$, the present device is not an ideal Chern insulator. Yet after early magnetically doped topological insulators showed comparable values (*39*–*41*), growth improvements in those materials soon yielded QAH (*24*–*26*). If the present device is a nascent Chern insulator, the largest measured $R_{yx}^{AH} \approx h/2.5e^2$ limits the possible Chern number to $C = 1$ or 2.

In combination with nonlocal transport that appears incompatible with homogeneous bulk conduction, the sheer magnitudes of the Hall and longitudinal resistances suggest a picture of chiral edge modes in combination with a poorly conducting bulk or a network of magnetic domain walls resulting from inhomogeneity [see (*17*) for additional discussion]. These possibilities can be directly explored in future experiments using spatially resolved magnetometry to search for domains and transport in a Corbino geometry to measure bulk conduction independent of chiral edge modes if domain walls can be removed.

Achieving a Chern insulator state by definition requires opening a topologically nontrivial gap. The low-energy flat minibands in magic-angle TBG are empirically isolated from higher order bands (*4*), which is expected when taking into account mutual relaxation of the two layers' lattices (*3*). The low energy conduction and valence minibands have been variously predicted to meet at Dirac points at the CNP, which may (*42*, *43*) or may not (*44*, *45*) be symmetry protected. The rotational alignment of the TBG to one of the hBN cladding layers in our device could thus be key to the observed AH effect: the associated periodic moiré potential should, on average, break A-B sublattice symmetry, opening or enhancing a gap at the mini-Dirac points. A gap associated with such symmetry breaking has been seen (*19*, *46*, *47*) and explained (*48*–*50*) in heterostructures of monolayer or Bernal-stacked bilayer graphene aligned with hBN. At ${}^3/_4$ filling of the

conduction band of thus-gapped magic-angle TBG, spin and valley symmetry may be spontaneously broken, and three of the four flavors filled with the other empty. This scenario could account for our observation of an apparent Chern insulator. Xie and MacDonald predict (*9*) a QAH effect arising in TBG (without aligned hBN) at $^{3}/_{4}$ filling from such a mechanism [see (*51*) for a prediction of a similar situation in graphene-based moiré systems].

Aside from the topological aspect, the appearance of magnetism in this system is notable. Unlike previous studies of graphitic carbon exhibiting magnetism owing to adsorbed impurities (*52*) or defects (*53*, *54*) [including (*55*), where the magnetism observed in bulk graphite has since been attributed to defects (*56*, *57*)], the order in the present device appears to emerge because of interactions in a clean graphene-based system; the AH signal appears only in a narrow range of densities around a state that may be spin and valley polarized. Such intrinsic magnetism also stands in contrast to the magnetic topological insulators, where exchange coupling is induced through doping with transition metals (*24*, *28*, *30*). Further experiments and theory will be needed to elucidate the order parameter, which may have both spin and orbital components or break spatial symmetry [compare with (*58*) for a model in which an antiferromagnet is a Chern insulator].

The discovery of a possible platform for QAH physics, less disordered than the familiar magnetic chalcogenide alloys, offers hope for more-robust quantization, with applications in metrology (*27*), quantum computation (*59*–*61*), or low-power-consumption electronics. The ability to switch the magnetization in TBG with an applied current might have practical applications in extremely low-power magnetic memory architectures, given the orders-of-magnitude smaller critical current density required for flipping the magnetization compared with prior devices (*36*). More broadly, understanding the magnetic order and topological character of the correlated insulating states will be crucial to unraveling the rich phase diagram of TBG.

Note added in proof: After submission of this manuscript, two theoretical works were made public (*62*, *63*) in which the alignment of TBG to a cladding hBN layer is specifically considered and possible mechanisms for ferromagnetism and an AH effect are discussed.

REFERENCES AND NOTES

1. R. Bistritzer, A. H. MacDonald, *Proc. Natl. Acad. Sci. U.S.A.* **108**, 12233–12237 (2011).
2. S. Fang, E. Kaxiras, *Phys. Rev. B* **93**, 235153 (2016).
3. N. N. Nam, M. Koshino, *Phys. Rev. B* **96**, 075311 (2017).
4. Y. Cao *et al.*, *Phys. Rev. Lett.* **117**, 116804 (2016).
5. Y. Cao *et al.*, *Nature* **556**, 80–84 (2018).
6. M. Yankowitz *et al.*, *Science* **363**, 1059–1064 (2019).
7. Y. Cao *et al.*, *Nature* **556**, 43–50 (2018).
8. J. Kang, O. Vafek, *Phys. Rev. Lett.* **122**, 246401 (2019).
9. M. Xie, A. H. MacDonald, On the nature of the correlated insulator states in twisted bilayer graphene. arXiv:1812.04213 [cond-mat.str-el] (11 December 2018).
10. M. Ochi, M. Koshino, K. Kuroki, *Phys. Rev. B* **98**, 081102 (2018).
11. J. F. Dodaro, S. A. Kivelson, Y. Schattner, X. Q. Sun, C. Wang, *Phys. Rev. B* **98**, 075154 (2018).
12. A. Thomson, S. Chatterjee, S. Sachdev, M. S. Scheurer, *Phys. Rev. B* **98**, 075109 (2018).
13. J. W. F. Venderbos, R. M. Fernandes, *Phys. Rev. B* **98**, 245103 (2018).
14. K. Seo, V. N. Kotov, B. Uchoa, *Phys. Rev. Lett.* **122**, 246402 (2019).
15. B. Padhi, P. Phillips, *Phys. Rev. B* **99**, 205141 (2019).
16. K. Kim *et al.*, *Nano Lett.* **16**, 1989–1995 (2016).
17. See supplementary materials.
18. J. B. Oostinga, H. B. Heersche, X. Liu, A. F. Morpurgo, L. M. K. Vandersypen, *Nat. Mater.* **7**, 151–157 (2008).
19. B. Hunt *et al.*, *Science* **340**, 1427–1430 (2013).
20. H. Yoo *et al.*, *Nat. Mater.* **18**, 448–453 (2019).
21. J. Xue *et al.*, *Nat. Mater.* **10**, 282–285 (2011).
22. S. Emori, C. K. Umachi, D. C. Bono, G. S. Beach, *J. Magn. Magn. Mater.* **378**, 98–106 (2015).
23. N. Nagaosa, J. Sinova, S. Onoda, A. H. MacDonald, N. P. Ong, *Rev. Mod. Phys.* **82**, 1539–1592 (2010).
24. C.-Z. Chang *et al.*, *Science* **340**, 167–170 (2013).
25. J. G. Checkelsky *et al.*, *Nat. Phys.* **10**, 731–736 (2014).
26. X. Kou *et al.*, *Phys. Rev. Lett.* **113**, 137201 (2014).
27. E. J. Fox *et al.*, *Phys. Rev. B* **98**, 075145 (2018).
28. R. Yu *et al.*, *Science* **329**, 61–64 (2010).
29. A. J. Bestwick *et al.*, *Phys. Rev. Lett.* **114**, 187201 (2015).
30. C.-Z. Chang *et al.*, *Phys. Rev. Lett.* **115**, 057206 (2015).
31. M. Büttiker, *Phys. Rev. B* **38**, 9375–9389 (1988).
32. L. J. van der Pauw, *Philips Res. Rep.* **13**, 1 (1958).
33. J. Wang, B. Lian, H. Zhang, S.-C. Zhang, *Phys. Rev. Lett.* **111**, 086803 (2013).
34. I. T. Rosen *et al.*, *npj Quantum Mater.* **2**, 69 (2017).
35. K. Yasuda *et al.*, *Science* **358**, 1311–1314 (2017).
36. D. Apalkov, B. Dieny, J. M. Slaughter, *Proc. IEEE* **104**, 1796–1830 (2016).
37. P. Upadhyaya, Y. Tserkovnyak, *Phys. Rev. B* **94**, 020411 (2016).
38. E. Liu *et al.*, *Nat. Phys.* **14**, 1125–1131 (2018).
39. J. G. Checkelsky, J. Ye, Y. Onose, Y. Iwasa, Y. Tokura, *Nat. Phys.* **8**, 729–733 (2012).
40. C.-Z. Chang *et al.*, *Adv. Mater.* **25**, 1065–1070 (2013).
41. X. Kou *et al.*, *ACS Nano* **7**, 9205–9212 (2013).
42. H. C. Po, L. Zou, A. Vishwanath, T. Senthil, *Phys. Rev. X* **8**, 031089 (2018).
43. L. Zou, H. C. Po, A. Vishwanath, T. Senthil, *Phys. Rev. B* **98**, 085435 (2018).
44. J. Kang, O. Vafek, *Phys. Rev. X* **8**, 031088 (2018).
45. M. Koshino *et al.*, *Phys. Rev. X* **8**, 031087 (2018).
46. F. Amet, J. R. Williams, K. Watanabe, T. Taniguchi, D. Goldhaber-Gordon, *Phys. Rev. Lett.* **110**, 216601 (2013).
47. F. Amet, thesis, Stanford University (2014).
48. P. Moon, M. Koshino, *Phys. Rev. B* **90**, 155406 (2014).
49. M. Mucha-Kruczyński, J. R. Wallbank, V. I. Fal'Ko, *Phys. Rev. B* **88**, 205418 (2013).
50. J. Jung, A. M. DaSilva, A. H. MacDonald, S. Adam, *Nat. Commun.* **6**, 6308 (2015).
51. Y.-H. Zhang, D. Mao, Y. Cao, P. Jarillo-Herrero, T. Senthil, *Phys. Rev. B* **99**, 075127 (2019).
52. N. Yeh, K. Sugihara, M. S. Dresselhaus, G. Dresselhaus, *Phys. Rev. B* **40**, 622–635 (1989).
53. P. Esquinazi *et al.*, *Phys. Rev. Lett.* **91**, 227201 (2003).
54. A. W. Mombrú *et al.*, *Phys. Rev. B* **71**, 100404 (2005).
55. Y. Kopelevich, J. C. Medina Pantoja, R. R. da Silva, F. Mrowka, P. Esquinazi, *Phys. Lett. A* **355**, 233–236 (2006).
56. J. Červenka, M. I. Katsnelson, C. F. J. Flipse, *Nat. Phys.* **5**, 840–844 (2009).
57. P. Esquinazi *et al.*, *AIP Adv.* **4**, 117121 (2014).
58. P. Zhou, C. Q. Sun, L. Z. Sun, *Nano Lett.* **16**, 6325–6330 (2016).
59. B. Lian, X.-Q. Sun, A. Vaezi, X.-L. Qi, S.-C. Zhang, *Proc. Natl. Acad. Sci. U.S.A.* **115**, 10938–10942 (2018).
60. Q. L. He *et al.*, *Science* **357**, 294–299 (2017).
61. A. C. Mahoney *et al.*, *Nat. Commun.* **8**, 1836 (2017).
62. N. Bultinck, S. Chatterjee, M. P. Zaletel, Anomalous Hall ferromagnetism in twisted bilayer graphene. arXiv:1901.08110 [cond-mat.str-el] (23 January 2019).
63. Y.-H. Zhang, D. Mao, T. Senthil, Twisted Bilayer Graphene Aligned with Hexagonal Boron Nitride: Anomalous Hall Effect and a Lattice Model. arXiv:1901.08209 [cond-mat.str-el] (24 January 2019).
64. A. L. Sharpe, E. Fox, A. Barnard, J. Finney, K. Watanabe, T. Taniguchi, M. Kastner, D. Goldhaber-Gordon, Data for: Emergent ferromagnetism near three-quarters filling in twisted bilayer graphene, Version 1.0, Stanford Digital Repository (2019); doi.org/10.25740/bg095cp1548.

ACKNOWLEDGMENTS

We thank M. Zaletel, A. MacDonald, M. Xie, T. Senthil, S. Kivelson, Y. Schattner, N. Bultinck, P. Gallagher, F. Wang, M. Yankowitz, and G. Chen for fruitful discussions. Y. Cao and P. Jarillo-Herrero generously taught us about their fab process and shared their insights into TBG. H. Schwartz and S. Yang helped with device fabrication and, along with A. Chen, performed preliminary measurements as part of a project-based lab class at Stanford. **Funding:** Device fabrication, measurements, and analysis were supported by the U.S. Department of Energy, Office of Science, Basic Energy Sciences, Materials Sciences and Engineering Division, under contract DE-AC02-76SF00515. Infrastructure and cryostat support were funded in part by the Gordon and Betty Moore Foundation through grant GBMF3429. Part of this work was performed at the Stanford Nano Shared Facilities (SNSF), supported by the National Science Foundation under award ECCS-1542152. A.L.S. acknowledges support from a Ford Foundation Predoctoral Fellowship and a National Science Foundation Graduate Research Fellowship. E.J.F. acknowledges support from an ARCS Foundation Fellowship. K.W. and T.T. acknowledge support from the Elemental Strategy Initiative conducted by the MEXT, Japan, and the CREST (JPMJCR15F3), JST. **Author contributions:** A.L.S. and J.F. fabricated devices. K.W. and T.T. provided the hBN crystals used for fabrication. A.L.S. and E.J.F. performed transport measurements. A.L.S., E.J.F., A.W.B., and J.F. analyzed the data. M.A.K. and D.G.-G. supervised the experiments and analysis. The manuscript was prepared by A.L.S. and E.J.F. with input from all authors. **Competing interests:** M.A.K. is a member of the science advisory board of the Gordon and Betty Moore Foundation and is chair of the Basic Energy Sciences Advisory Committee. Both the Moore Foundation and Basic Energy Sciences provided funding for this work. **Data and materials availability:** The data from this study are available at the Stanford Digital Repository (*64*).

SUPPLEMENTARY MATERIALS

science.sciencemag.org/content/365/6453/605/suppl/DC1
Materials and Methods
Supplementary Text
Figs. S1 to S10
References (*65*–*70*)

15 December 2018; accepted 3 July 2019
Published online 25 July 2019
10.1126/science.aaw3780

Emergent ferromagnetism near three-quarters filling in twisted bilayer graphene

Aaron L. Sharpe, Eli J. Fox, Arthur W. Barnard, Joe Finney, Kenji Watanabe, Takashi Taniguchi, M. A. Kastner and David Goldhaber-Gordon

Science **365** (6453), 605-608.
DOI: 10.1126/science.aaw3780originally published online July 25, 2019

Twisted bilayer graphene goes magnetic

When two layers of graphene in a bilayer are twisted with respect to each other by just the right, "magic," angle, the electrons in the system become strongly correlated. As the electronic density is tuned by gating, the system goes through several exotic phases, including superconductivity. Now, Sharpe *et al.* show that, at a particular electronic density, magic-angle graphene becomes magnetic (see the Perspective by Pixley and Andrei). The finding is supported by the observation of a large anomalous Hall effect.

Science, this issue p. 605; see also p. 543